Statistical Digital Predistortion of 5G Millimeter-Wave RF Beamforming Transmitter Under Random Amplitude Variations

Bilal Khan, *Graduate Student Member, IEEE*, Nuutti Tervo, *Member, IEEE*, Markku Jokinen, Aarno Pärssinen, *Senior Member, IEEE*, and Markku Juntti, *Fellow, IEEE*

***Abstract*— The nonlinearity of the fifth-generation (5G) millimeter-wave (mmWave) phased array transmitter (TX) depends on the variations in the beamforming coefficients, e.g., due to unwanted amplitude errors of the phase shifters or purposely introduced amplitude variations to shape the beam, as well as other analog component variations. Therefore, also the digital predistortion (DPD) coefficients depend on the beamforming coefficients and require a continuous update for different beamsteering directions in a conventional DPD. We propose a robust DPD approach that uses the average array response for DPD training. The average array response is estimated using the known experimental histogram of power amplifier (PA) input power variation resulting from the amplitude variations due to beamforming. The DPD training based on the average array response makes the DPD coefficients insensitive to beamforming variations. The proposed DPD strategy requires a shared feedback path for training and only a single set of DPD coefficients to linearize the array response in all beamsteering directions. The performance of the proposed DPD strategy is validated by over-the-air (OTA) measurements of a 28-GHz phased array TX over different steering angles. Experimental results show that the proposed DPD method using one set of DPD coefficients provides similar linearization performance across the steering angles compared with the DPD trained to all steering angles through the OTA reference antenna.**

***Index Terms*— Beamforming, digital predistortion (DPD), fifth-generation (5G), millimeter-wave (mmWave), over-the-air (OTA), power amplifier (PA) linearization.**

I. Introduction

MILLIMETER-WAVE (mmWave) frequency bands are envisioned to fulfill the high data rates promised by the fifth-generation (5G) wireless systems [1] and will have a major role in sixth-generation (6G) systems [2]. The mmWave systems rely on the dense integration of multiple antenna elements to overcome the high path loss at such frequency bands [3]. Multiple-input–multiple-output (MIMO) systems and phased transmit and receive arrays are, therefore, necessary in mmWave systems. This means that the major part of the beamforming is implemented in the radio frequency (RF) domain by varying the phase and amplitude of the signal in each antenna path. With appropriate beamforming coefficients, the radiated power is dynamically focused to users in different directions to overcome the excessive path loss and ensure reliable connectivity.

Phased array transmitters (TXs) are equipped with a shared digital input and multiple parallel power amplifiers (PAs) that drive the antenna elements. The PAs being the dominant component in terms of power consumption dictate the overall efficiency of the TX. Thus, the PAs of the array are required to be operated close to their saturation to achieve better efficiency [4]. However, the highly efficient PAs have inherently nonlinear characteristics that affect the transmitted signal quality, therefore degrading the bit error rate (BER). Also, the nonlinear distortion of the PA introduces interference to users in adjacent frequency bands.

Digital predistortion (DPD) has been widely used to correct the impairments of PA in third-generation (3G) and fourth-generation (4G) systems because of its low-cost implementation [5]–[8]. However, in mmWave systems, DPD implementation is challenging and under active research. In phased arrays, used heavily in the mmWave systems, the input of each parallel PA cannot be accessed independently. Thus, a single-input–single-output (SISO) DPD block has to linearize all the parallel PA branches. In phased arrays, the nonlinear characteristics of parallel PA branches are not identical compared with each other. Furthermore, the PA branch nonlinear characteristics are varying over time when the array is transmitting to different steering directions in different time instants. Consequently, the array nonlinear behavior varies over the steering angles complicating the adaptation of the SISO DPD coefficients. The variation in the nonlinear characteristics of the parallel PA branches can be attributed to the following static and dynamic sources. The static ones include the variations in the PA design and the fabrication or the imbalances in the power division network. The dynamic

Manuscript received 19 January 2022; revised 30 April 2022; accepted 12 June 2022. Date of publication 14 July 2022; date of current version 7 September 2022. This work was supported in part by the Wireless Connectivity for Internet of Everything Energy Efficient Transceiver and System Design (WiConIE), in part by the Energy-Efficient Radio Access: Methods and Optimization (EERA), and in part by the Academy of Finland 6Genesis Flagship under Grant 318927. This article has been presented in part at the 2019 IEEE 30th Annual International Symposium on Personal, Indoor and Mobile Radio Communications (PIMRC), Istanbul, Turkey, Sept 8-11, 2019 [DOI: 10.1109/PIMRC.2019.8904111]. *(Corresponding author: Bilal Khan.)*

The authors are with the Center for Wireless Communications–Radio Technologies (CWC-RT), Faculty of Information Technology and Electrical Engineering (ITEE), University of Oulu, 90570 Oulu, Finland (e-mail: bilal.khan@oulu.fi).

Color versions of one or more figures in this article are available at https://doi.org/10.1109/TMTT.2022.3187129.

Digital Object Identifier 10.1109/TMTT.2022.3187129

sources of variation include the variations in PA nonlinearity over the steering angles due to load pulling from the neighboring antennas, the PA input power variations caused by the amplitude errors of the phase shifters [9]–[11], or the purposely introduced PA input power variations, e.g., in zero-forcing (ZF) beamforming or maximum ratio transmission (MRT), depending on the radio channel conditions. These variations in the nonlinear characteristics of the parallel PA branches cause the overall radiated array nonlinear behavior to be direction-dependent [11]–[14].

Several strategies have been presented in the literature to optimize the SISO DPD performance and its implementation for array linearization. Prior work of phased array linearization through a single DPD block that uses a timely shared feedback path includes [15]–[18]. In [19] and [20], weighted analog feedback networks are used to emulate the array far-field behavior. In addition, Ng *et al.* [11], Tervo *et al.* [12], Hausmair *et al.* [21], and Wang *et al.* [22] use a far-field observation receiver (RX) to measure the array far-field response that is used with the common digital input signal for DPD training. DPD approaches based on the array far-field response minimize the nonlinear distortion in the direction of interest, i.e., the beamforming direction.

The existing literature related to the SISO DPD for array offers a good linearization performance with experimental verification. However, the variations in the radiated array nonlinear behavior over the steering angles impose continuous adaptation of the SISO DPD coefficients. Updating the DPD coefficients for every steering angle requires continuous training either in real-time or in dedicated training periods. Especially if the steering angle changes randomly for every slot, very fast DPD adaptation is required to enable good linearity. Therefore, in [23], linearization angle broadening was proposed to increase the linearized azimuth angle interval. However, the reported performance is limited up to 10° sector of linearized angles. Similarly, Ng *et al.* [11] propose to use more than one over-the-air (OTA) RX spatially distributed across the azimuth angular range to train the DPD coefficients for a subset of angular directions. The reported linearization performance is up to 20°–40° sector of linearized angles per OTA RX. However, the approaches in [11] and [23] rely on array far-field response measurement from different spatially distributed directions. Furthermore, Liu *et al.* [24] used a coupling antenna within the actual TX antenna array, to measure PA branch responses, whereas Wang *et al.* [25] used an OTA RX antenna at a fixed location to identify individual PA branch models and ultimately estimate the array far-field response for identifying the predistorter. However, the reported work lacks to address the PA input power variation due to the RF components or the intended beamforming with non-unitary amplitudes across the PA inputs. The PA input power variations result in the variation in the radiated array nonlinear response, and therefore impose retraining of the DPD coefficients continuously even with perfect antenna isolation.

When the steering angle is random, also the variations in the DPD coefficients become random [26]. Using this assumption, an SISO-based statistical DPD (SDPD) approach was presented in [27] that can tolerate the changes in the array nonlinear response due to the rapid changes in beamsteering directions with no need for DPD coefficients readaptation. The SDPD approach uses the PA input power variations resulting from beamforming variations, to approximate the average array response for DPD model training. The used approach provides decent linearization performance to the spatially distributed user directions through only one-time trained DPD coefficients. However, the reported analysis in [27] was based on the assumption that all PAs of the array exhibit similar nonlinear characteristics, and the analysis was limited to simulations only. In this article, we extend the concept of [27] to cover also the variations in individual PA models and provide the theoretical basis for array nonlinear behavior dependency on beamforming variations. The overall concept is demonstrated on an mmWave hardware platform with extensive set of OTA measurements using 5GNR waveform.

This article is organized as follows. Section II presents the theoretical background of the array nonlinear behavior dependency on beamforming variations. The proposed SDPD derivation is presented in Section III. A simulation example of the linearization performance of the proposed DPD method along with two other DPD strategies in the presence of beamforming variations is presented in Section IV. OTA measurement setup and experimental validation of the proposed DPD method are explained in Section V with conclusions in Section VI.

II. Radiated Nonlinear Distortion of Amplitude-Varying Phased Arrays

In this section, we present the theoretical analysis of the impact of beamformer amplitude variations on the nonlinear behavior of the phased array TXs.

A. System Model

In phased arrays, a common digital input is shared among the parallel PA branches. The individual PA branches are equipped with phase shifters to perform the required beamsteering. The phase shifters have inherent control word-dependent gain, which causes variations in the input power of the PA, therefore changing the PA nonlinear behavior. The amplitude error varies from fractions of dBs to even several dBs depending on the technology. As a result, the overall PA array nonlinear behavior slightly varies when transmitting to different spatial directions.

Let us demonstrate the radiated array nonlinear distortion variation with a simulation example. The block diagram of the simulated phased array is shown in Fig. 1. The PA nonlinear functions f_{PA} are memory polynomial (MP) models extracted from the modulated signal measurements of 16 different TGA2595 GaN PAs in a 28-GHz phased array platform [28]. In addition, the PA input power variations resulting from the amplitude errors of 16 different TGP2100 5-b phase shifters are measured. Traditionally, in phased arrays, access to PA input signal is not available, and only PA output can be measured. In practice, the change in the input power of the PA due to the phase shifter amplitude errors is relatively small, and

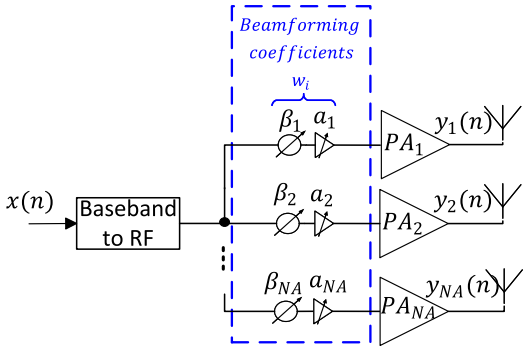

Fig. 1. System diagram of phased array with amplitude-varying beamforming.

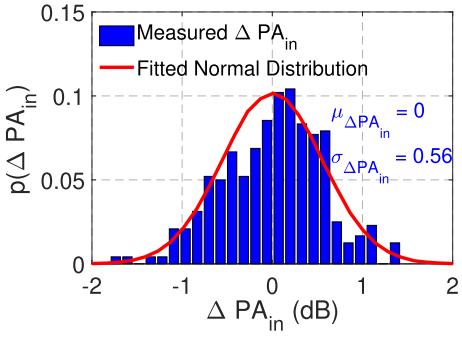

Fig. 2. Experimental histogram of the normalized PA input power measured from 16 parallel transmit paths. The variation is due to phase shifters' amplitude errors.

it does not affect the linear gain of the PA significantly. Hence, it is safe to assume that the power variation measured at the PA output is the same as the power variation that happens at the input of the PA due to the phase shifter states. The distribution of the measured PA input power variations resulting from 16 phase shifters along with the fitted theoretical normal distribution is shown in Fig. 2. The polynomial models of the PAs, along with the PA input power variation resulting from phase shifters, are used in the phased array of Fig. 1. Uniform rectangular array (URA) having 16 different λ spaced patch elements in 8×2 configuration are used. The array input signal is represented by $x(n)$, $n = 1, 2, 3, \ldots, N$ is the sampling index, and N is the total number of samples. $x(n)$ is 100-MHz wide, 64 quadrature-amplitude-modulated (QAM) cyclic-prefix (CP) orthogonal frequency division multiplexing (OFDM) signal. The output signal of the ith branch PA is given as

$$y_i(n) = f_{\text{PA}i}(w_i x(n)) \tag{1}$$

$$w_i(n) = a_i e^{(j\beta_i)} \tag{2}$$

where $y_i(n)$ is the ith branch output, $f_{\text{PA}i}$ is the nonlinear function modeling the PA in the ith branch, β_i represents the progressive phase shift, and a_i represents the amplitude errors associated with the phase shifter in the ith branch. Representing the nonlinear function of PA by an MP model leads to

$$y_i(n) = \sum_{\substack{p=1 \\ p=\text{odd}}}^{P} \sum_{m=0}^{M} c_{p,m,i} w_i x(n-m) |w_i x(n-m)|^{(p-1)} \tag{3}$$

where $c_{p,m,i}$ represents the PA coefficients in the ith branch, P is the polynomial order, and M represents the memory length. The individual branch responses are coherently combined OTA, and the received signal at a user location in the elevation and azimuth direction $(\theta_\circ, \phi_\circ)$ is $y_{\text{RX}}(n, \theta_\circ, \phi_\circ)$ and it is given by

$$\begin{aligned} &y_{\text{RX}}(n, \theta_o, \phi_o) \\ &= \sum_{i=1}^{N_\text{A}} \sum_{\substack{p=1 \\ p=\text{odd}}}^{P} \sum_{m=0}^{M} \\ &\quad \times c_{p,m,i} a_i e^{(j\beta_i)} x(n-m) a_i^{(p-1)} |x(n-m)|^{(p-1)} e^{j\mathbf{k}^T \mathbf{r}_i} \end{aligned} \tag{4}$$

$e^{j\beta_i} e^{j\mathbf{k}^T \mathbf{r}_i} = 1$ for coherent combining in the channel

$$\begin{aligned} &y_{\text{RX}}(n, \theta_o, \phi_o) \\ &= \underbrace{\sum_{i=1}^{N_\text{A}} \sum_{m=0}^{M} c_{1,m,i} a_i x(n-m)}_{\text{linear signal}} \\ &\quad + \underbrace{\sum_{i=1}^{N_\text{A}} \sum_{\substack{p=3 \\ p=\text{odd}}}^{P} \sum_{m=0}^{M} c_{p,m,i} a_i x(n-m) a_i^{(p-1)} |x(n-m)|^{(p-1)}}_{\text{nonlinear signal}} \end{aligned} \tag{5}$$

where $N_\text{A} = 16$ is the total number of parallel PA branches, $\mathbf{k} = (2\pi/\lambda)[\sin(\theta_\circ)\cos(\phi_\circ), \sin(\theta_\circ)\sin(\phi_\circ), \cos(\theta_\circ)]^T$, $\mathbf{k} = [k_x, k_y, k_z]^T$, $\mathbf{k} \in \mathbb{R}^3$ denotes the 3-D wave vector, $(.)^T$ denotes the transpose, and $\mathbf{r}_i = [r_x, r_y, r_z]^T$, and $\mathbf{r}_i \in \mathbb{R}^3$ denotes the ith antenna element coordinates in the Cartesian coordinate system.

Equation (5) represents the array far-field response and it can be used as the output measurement for the array coefficients or SISO DPD coefficients' extraction. The amplitude errors in the ith branch a_i cause the PA input power to change. Thus, the vector of basis function of the PA models representing linear part experience multiplication by a_i, whereas the vectors of basis function of the PA models representing the nonlinear part experience multiplication by $a_i a_i^{(p-1)}$ (for $p \geq 3$). This means that the individual PA response (linear and nonlinear) and eventually the array response (linear and nonlinear) is a function of the amplitude errors of the phase shifters. To further demonstrate array response dependency on the amplitude errors, we performed Monte Carlo (MC) simulations over 1000 trials. In each MC trial, the ith branch PA input power is the sum of power of common branch input signal $x(n)$ and a random value of power variation ($\Delta\text{PA}_{\text{in},i}$ due to amplitude errors) drawn from the fitted normal distribution of Fig. 2 and its impact on the array response is observed. Fig. 3 shows the distribution of the magnitude of array coefficients in dB scale. The figure shows that the first-order polynomial coefficients ($p = 1$) of the array do not vary significantly, but as we move up the order of the

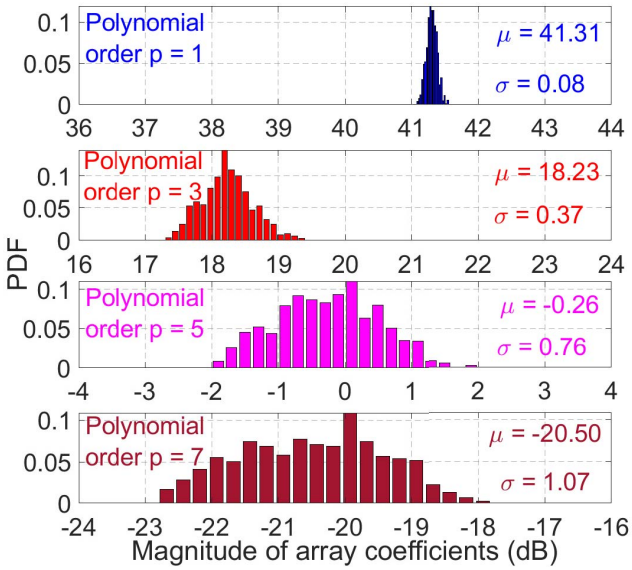

Fig. 3. Simulated histograms of the magnitude of array nonlinear coefficients in dB scale. The amount of variation is larger for higher order terms than that of lower order terms.

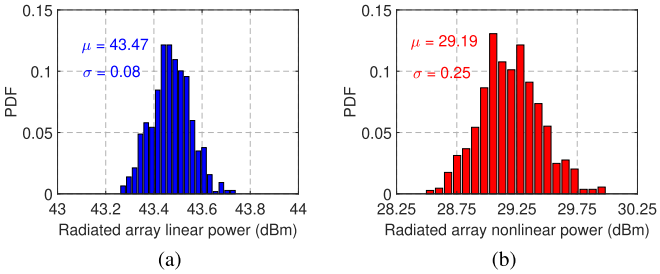

Fig. 4. Simulated histograms of (a) radiated array linear power and (b) radiated array nonlinear power with random input amplitude errors, respectively.

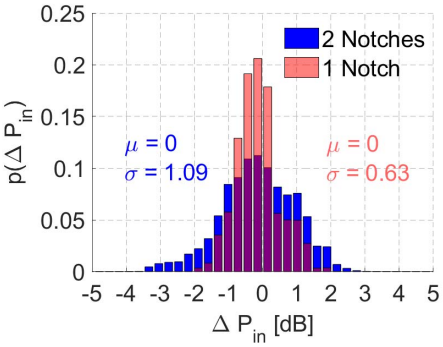

Fig. 5. Simulated histograms of the input power variation of 16 parallel PA branches while performing ZF beamforming with one and two nulls. In all the cases, the main lobe is steered toward the intended user.

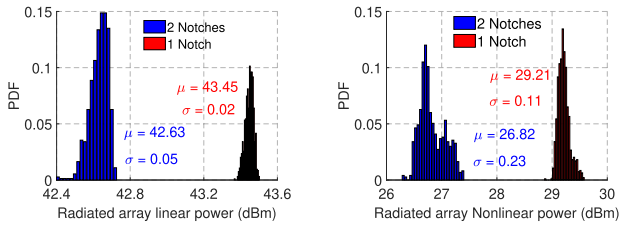

Fig. 6. Simulated histograms of (a) radiated array linear power and (b) radiated array nonlinear power with ZF beamforming.

polynomial, the spread in the array nonlinear coefficients ($p \geq 3$) becomes significant. This means that for a highly nonlinear array of PAs, even a small variation at the input can have a significant impact on the array nonlinearity. A similar trend is seen for the phase of the array coefficients though not presented here. Furthermore, Fig. 4 shows the distribution of the radiated array linear power OTA and radiated array nonlinear power OTA as a function of the PA input power variation due to amplitude errors of the phase shifters.

It is worth noting that the variation in the radiated array nonlinear behavior is not limited to unwanted amplitude errors of the phase shifters, which might be small, especially in well-calibrated and highly integrated systems. For example, the variation in the array nonlinear behavior can also occur in scenarios where purposely made amplitude variations are introduced when more advanced beamforming methods other than simple beamsteering are used. For example, performing ZF beamforming over subarrays in partially connected hybrid beamforming (HBF) architectures used in multiuser MISO systems [29]. In subarray-based processing of partially connected HBF architecture, each subarray serves one user and performs ZF beamforming to its corresponding user by varying the input amplitude and phase of individual branches in the subarray and nulling interference to other users. These amplitude variations cause PA input power to vary and therefore change its nonlinear behavior. Fig. 5 shows the distribution of PA input power variation resulting from the amplitude variations required to perform ZF beamforming for an URA having λ spaced 16 elements in 8×2 configuration. The power variation distribution is a result of MC simulations over 10 000 random trials. In each MC trial, steering angle and a null direction are randomly selected from the range $\phi_s \in \bigcup(-30°,\ 30°)$ in the azimuth domain. The null direction is kept 10° degree away from the main beam.

Fig. 6 shows the distribution of radiated array linear and nonlinear power while performing ZF beamforming. It should be noted that for the case of two notches, the root-mean-square (rms) power of the common input signal of the array is kept 1 dB lower in comparison to the case of one notch, to be able to use the larger power variations required for ZF beamforming. The linear array gain variation is normalized out in the process of DPD coefficient calculation. However, the radiated array nonlinear power variation necessitates the DPD coefficients retraining to adapt to the varying nonlinearity. This is because together with DPD linearization, small nonlinear variation in the trained operation point can have a significant impact on the overall DPD performance.

III. SDPD Architecture for Phased Array Linearization

The block diagram of the SDPD for phased array is shown in Fig. 7. In practical systems, the PAs of the array exhibit different nonlinear characteristics from one another due to

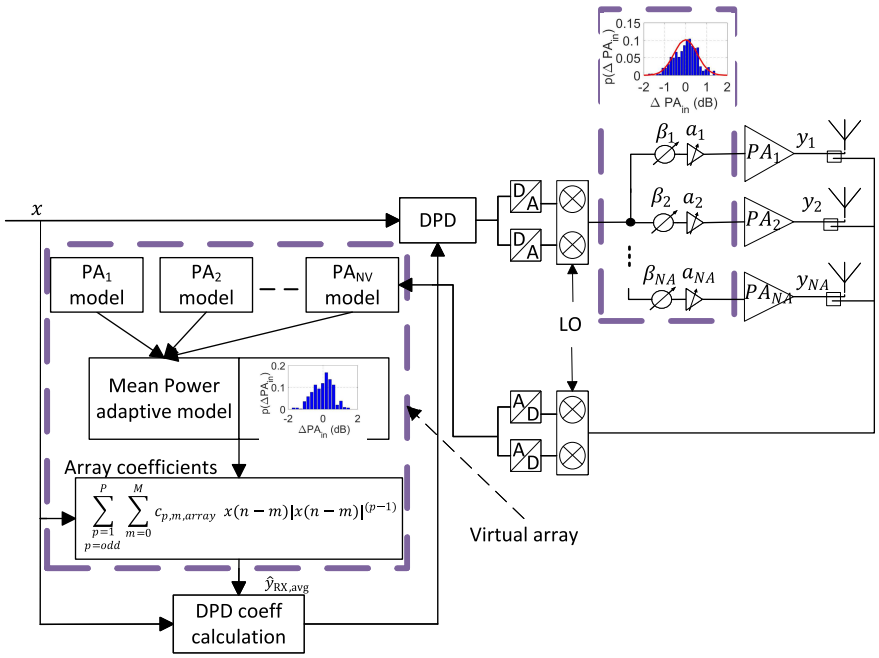

Fig. 7. Block diagram of SDPD for phased arrays including beamforming variations. The distribution of beamforming variations is sampled in the virtual array block and used along with the mean power adaptive model to estimate the average array response $y_{\text{RX,avg}}$ for DPD model training.

the variations in their design and fabrication. In addition, the power variations introduced by the phase shifter control word dependent gain drives the PAs in different operating points. The SDPD uses the statistical information of the power variations along with the mean power adaptive model of the array calculated through a shared feedback path and performs linearization of the array.

A. Mean Power Adaptive Modeling

The power variations due to phase shifters in the parallel PA branches of the phased array change the input power of the PA thus changing its nonlinear behavior. Conventionally, the PA behavior modeling is carried out using polynomial models, which are valid at one input power level for which it is estimated. When the input power of the PA changes, the nonlinear behavior of the PA also changes. To cope with this, the PA output response is often remeasured, and the behavior model of the PA (and the DPD coefficients) is recalibrated. Due to multiple PA branches, the system requires a much longer time period (with shared feedback path [18]), or more complicated DPD mechanisms [12], [19] to remeasure and recalibrate the nonlinear models. This can be addressed using a power adaptive modeling approach. The aim of such modeling for arrays is to make the model of each PA branch tolerate the uncertainty of the PA input power. The concept of power adaptive modeling was introduced in [30] for standalone PA linearization in systems where adaptive TX power control is used. Here, we use the power adaptive modeling concept along with the statistical information of the input power variation in the parallel PA branches to predict the average array response. The SDPD object is estimated from the predicted average array response.

The power adaptive model of any ith PA branch is created as follows. The common branch input signal $x(n)$ has fixed rms power. The signal power changes when passed through the phase shifter before the PA due to the amplitude variation associated with the phase shifter states. The range of the PA input power variation is quantized into L points, $P_{l,i}$, $l \in \{1, 2, \ldots, L\}$ such that $P_{1,i} > P_{2,i} > \cdots > P_{L,i}$, where i is the branch index. The ith branch PA coefficients at any given input power $P_{l,i}$ can be updated as a function of power back-off from the PA coefficients at maximum input power $P_{1,i}$ as

$$\mathbf{c}_i^{(l)} = \hat{\mathbf{c}}_i + \Delta\mathbf{c}_i^{(l)} \tag{6}$$

where

$$\Delta\mathbf{c}_i^{(l)} = \begin{bmatrix} \alpha_{\text{lin},i}^{(l)} & \Delta\mathbf{c}_{\text{lin},i} \\ \alpha_{\text{n-lin},i}^{(l)} & \Delta\mathbf{c}_{\text{n-lin},i} \end{bmatrix} \tag{7}$$

$$\alpha_{\text{lin},i}^{(l)} = G_{l,i} - G_{1,i}, \quad \alpha_{\text{n-lin},i}^{(l)} = \gamma_{l,i} - \gamma_{1,i} \tag{8}$$

and

$$\gamma_{l,i} = \sqrt{\frac{\sum_{n=1}^{N} \left| y_i^{(l)}(n) - G_{l,i}\, x(n) \right|^2}{\sum_{n=1}^{N} \left| y_i^{(l)}(n) \right|^2}}. \tag{9}$$

In (6), $\hat{\mathbf{c}}_i$ is the coefficient vector of the ith PA at reference input power level $P_{1,i}$, i.e., maximum PA input power in the ith branch. The PA behavioral change when the PA input power changes from $P_{1,i}$ to $P_{l,i}$ is represented by $\Delta\mathbf{c}_i^{(l)}$. $\hat{\mathbf{c}}_i$ is the static part, whereas $\Delta\mathbf{c}_i^{(l)}$ is the dynamic part. In (7), a common set of coefficients $\Delta\mathbf{c}$ are extracted along with the dynamic scaling factors $\alpha_{\text{lin},i}^{(l)}$ and $\alpha_{\text{n-lin},i}^{(l)}$. The dynamic scaling factors

are power-dependent, whereas the common set of coefficients $\Delta\mathbf{c}_i$ are independent of power. The coefficient vector $\Delta\mathbf{c}_i$ has linear and nonlinear parts as $\Delta\mathbf{c}_{\text{lin},i}$ and $\Delta\mathbf{c}_{\text{n-lin},i}$, respectively, which are scaled accordingly by the dynamic scaling factors as shown in (7). The linear scaling factor $\alpha^{(l)}_{\text{lin},i}$ is the PA gain difference at power level $P_{l,i}$ and reference power level $P_{1,i}$, whereas the nonlinear scaling factor $\alpha^{(l)}_{\text{n-lin},i}$ is the difference in the degree of nonlinearity of the PA at power level $P_{l,i}$ and reference power level $P_{1,i}$. The measure of nonlinearity (MoN) is represented by γ. $y^{(l)}_i(n)$ is the PA output signal at power level $P_{l,i}$, $x(n)$ is the common branch input signal, n is the sampling index, and N is the total number of time-domain samples.

Following the same procedure, we can calculate the power adaptive model of each PA branch of the array. There are four parameters of the power adaptive model per branch, i.e., $\hat{\mathbf{c}}_i$, $\Delta\mathbf{c}_i$, $\alpha^{(l)}_{\text{lin},i}$, and $\alpha^{(l)}_{\text{n-lin},i}$. The mean power adaptive model is calculated by averaging the parameters of the power adaptive model of all the parallel PA branches as

$$\hat{\mathbf{c}} = \frac{1}{N_\text{A}}\sum_{i=1}^{N_\text{A}} \hat{\mathbf{c}}_i \tag{10}$$

$$\Delta\mathbf{c} = \frac{1}{N_\text{A}}\sum_{i=1}^{N_\text{A}} \Delta\mathbf{c}_i \tag{11}$$

$$\alpha^{(l)}_{\text{lin}} = \frac{1}{N_\text{A}}\sum_{i=1}^{N_\text{A}} \alpha^{(l)}_{\text{lin},i} \tag{12}$$

$$\alpha^{(l)}_{\text{n-lin}} = \frac{1}{N_\text{A}}\sum_{i=1}^{N_\text{A}} \alpha^{(l)}_{\text{n-lin},i} \tag{13}$$

where N_A is the total number of PA branches.

B. Statistical PA Array Model Training

The mean power adaptive model is used along with the experimental histogram of the PA input power variations among the parallel PA branches to predict the average array response as shown in the virtual block of Fig. 7. The distribution of the power variation due to 16 different 5-b TGP2100 phase shifters was presented in Section II-A in Fig. 2. This means that at any given time instant, the input power to the ith PA is equal to the power of the common branch input signal + $\Delta\text{PA}_\text{in}$ from the distribution resulting from phase shifters. In the virtual array of Fig. 7, the measured range of the PA input power variation is divided into equally spaced N_V intervals, and a predefined value is drawn from each interval as shown in Fig. 8. For average array response estimation, we assume that the number of equally spaced intervals of the histogram is equal to the number of array elements, i.e., $N_\text{V} = N_\text{A}$ [27]. The mean power adaptive model is considered as one virtual PA which is excited by an input signal with different power levels. The different power levels are the sum of the power of common branch input signal and sample values ($\Delta\text{PA}_\text{in}$) drawn from the histogram of the PA input power variation. The virtual PA coefficients provided by the mean power adaptive model are scaled according to the scaling factor obtained from the probability of occurrence

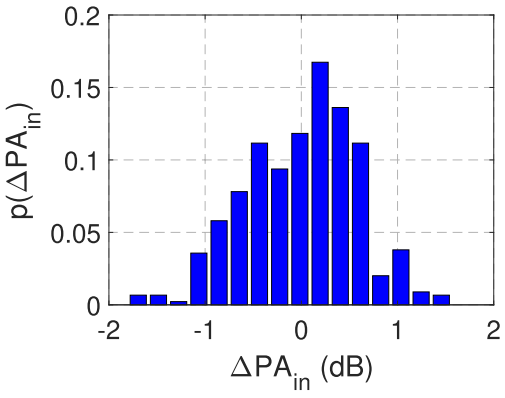

Fig. 8. Experimental histogram of PA input power variation (due to phase shifters amplitude errors) is divided into equally spaced 16 intervals.

of $\Delta\text{PA}_\text{in}$ as

$$S(\Delta\text{PA}_{\text{in},j}) = \frac{p(\Delta\text{PA}_{\text{in},j})}{\sum_{j=1}^{N_\text{V}} p(\Delta\text{PA}_{\text{in},j})} N_\text{V} \tag{14}$$

where $p(\Delta\text{PA}_{\text{in},j})$ is the probability of occurrence of $\Delta PA_{\text{in},j}$, and j is the sampling index. The virtual PA coefficients are combined to form the virtual array coefficients as

$$c_{p,m,\text{array}} = \sum_{j=1}^{N_\text{V}} c^{(l)}_{p,m} S(\Delta\text{PA}_{\text{in},j}) \tag{15}$$

where $c^{(l)}_{p,m}$ denotes the virtual PA coefficients obtained from the mean power adaptive model at power level l which is equal to the sum of rms power of common branch input signal and the jth sample from the power variation histogram. p is the index of order of the polynomial and m is the index for memory depth. It is important to note that the virtual PA coefficients are independent of where the actual PAs in the phased array are operating. The idea is to define virtual PAs at some fixed power levels in the virtual array such that the virtual array provides an estimate of the average array response of the phased array even when the behaviors of the PAs in the phased array are unknown and varying. Finally, the predicted average array far-field response is given by

$$\hat{y}_{\text{RX,avg}}(n) = \sum_{\substack{p=1\\ p=\text{odd}}}^{P}\sum_{m=0}^{M} c_{p,m,\text{array}} x(n-m)|x(n-m)|^{(p-1)}. \tag{16}$$

It is worth noting that the presented methodology requires an offline training period where individual PA branch measurements are performed for power adaptive modeling. To acquire an individual PA branch response, conductive feedback such as timely shared feedback or radiated feedback such as OTA RX antenna can be used. As it is required to measure one PA branch response at a time, the OTA RX antenna can be placed at a fixed location. In the case of timely shared feedback architecture, it might be impractical to couple each PA output to the shared feedback line due to dense integration. However, in large arrays, the array response tends to be more predictable due to the law of large numbers [27]. Therefore, the average behavior of the array could be estimated by measuring a subgroup of the parallel PA branches. This is because the objective

of the proposed methodology is to accurately estimate the average array response for DPD training rather than estimating individual PA responses with good accuracy.

C. DPD Coefficients Extraction

The predicted average array response is used along with the common branch input signal $x(n)$ to estimate the array DPD coefficients. The predistorter model is an MP model with the order of polynomial $P = 9$ and memory depth $M = 5$, similar to that of the mean power adaptive model. The predistorter input signal $x(n)$ can be written as

$$x(n) = \sum_{\substack{p=1 \\ p=\text{odd}}}^{P} \sum_{m=0}^{M} d_{p,m} \hat{y}_{\text{RX,avg}}(n-m) |\hat{y}_{\text{RX,avg}}(n-m)|^{(p-1)} \tag{17}$$

where $\mathbf{d} = [d_{1,1}, d_{1,2}, \ldots, d_{1,M}, \ldots, d_{P,M}]$, and $\mathbf{d} \in \mathbb{C}^{PM \text{ x } 1}$ denotes the DPD coefficient vector. $\hat{y}_{\text{RX,avg}}(n)$ is the array response predicted by (16). The problem can be written into matrix form and solved by least squares (LS) estimation as

$$\mathbf{d} = (\mathbf{Y}_{\text{RX,avg}}^{H} \mathbf{Y}_{\text{RX,avg}})^{-1} \mathbf{Y}_{\text{RX,avg}}^{H} \mathbf{x} \tag{18}$$

where $\mathbf{Y}_{\text{RX,avg}} \in \mathbb{C}^{N \text{ x } PM}$ includes all the product terms of $\sum_{\substack{p=1 \\ p=\text{odd}}}^{P} \sum_{m=0}^{M} \hat{y}_{\text{RX,avg}}(n-m) |\hat{y}_{\text{RX,avg}}(n-m)|^{(p-1)}$ of (17), $\mathbf{x} \in \mathbb{C}^{N}$ is the common input signal, N is the number of time-domain samples, and $(.)^{H}$ denotes the Hermitian transpose.

IV. Simulation Example of DPD Performance in the Presence of Amplitude-Varying Beamforming

In this section, the impact of the radiated array nonlinearity variation on the DPD performance is analyzed through simulations. The DPD performance in terms of adjacent channel power ratio (ACPR) is analyzed with three DPD training mechanisms. The three DPD training mechanisms are: 1) fixed-angle DPD; 2) main-lobe DPD; and 3) SDPD. In 1), the DPD coefficients are trained based on one realization of array response, i.e., from a fixed steering location $\phi_s = 0°$ in the azimuth domain, and the same DPD coefficients are used while the array beam is steered to different directions. In 2), the DPD coefficients are trained for each steering direction by calculating the OTA array response in the array main lobe. In 3), the proposed statistical training mechanism is used to estimate one set of DPD coefficients and use it for all steering directions. For all three training methods, the DPD is an MP model with polynomial order of 9 and a memory depth of 5. MC simulations over 1000 trials were performed. In each MC trial, the steering angle is selected from the range $\phi_s \in \bigcup(-30°,\ 30°)$ in the azimuth domain. In the case of PA input power variations due to phase shifters, each steering angle is associated with random parallel PA input power variation values, drawn from the fitted normal distribution of Fig. 2, and the three DPD performances were tested. On the other hand, in the case of ZF beamforming, the PA input powers are adjusted to steer the nulls in specific directions. For ZF beamforming, the PA input power variations follow the distribution of Fig. 5.

Fig. 9 shows the cumulative distribution function (cdf) of the tested DPD performance in terms of $\text{ACPR}_{\text{lower-ch}}$ and $\text{ACPR}_{\text{upper-ch}}$. From the figure, it can be seen that the fixed-angle DPD performance deteriorates since it is trained with only one realization of the array response. With the amplitude errors of the phase shifters, the array nonlinear behavior varies, and thus, the fixed-angle DPD coefficients become invalid. On the other hand, SDPD training is based on the estimated average array response, and using one set of DPD coefficients provides comparable performance to that of the main-lobe DPD without the necessity of updating its coefficients with varying array nonlinear behavior.

Similarly, the performance of the three tested DPD methods is evaluated in the scenario where ZF beamforming is performed. In this case, two nulls are steered to random directions selected from the range $(-30°,\ 30°)$ in the azimuth domain. The two nulls' direction is kept 10° away from the direction of the main beam of the array. Here, it is assumed that the phase shifters have no amplitude variations. All the amplitude variations are purposely introduced to perform the required ZF beamforming as presented in Section II-A. Fig. 10 shows the cdf of the tested DPD performance in terms of $\text{ACPR}_{\text{lower-ch}}$ and $\text{ACPR}_{\text{upper-ch}}$ in the presence of ZF beamforming. From the figure, it can be seen that the SDPD outperforms the fixed-angle DPD and provides comparable linearization performance to that of the main-lobe DPD.

V. Experimental Validation Through mmWave OTA Measurements

In this section, the SDPD for phased array is validated with OTA measurements of a 28-GHz phased array transceiver.

A. 28-GHz Phased Array Transceiver

The demonstration platform is a mmWave phased array RF front-end with 16 parallel TX/RX branches operating at 26.5–29.5 GHz [28], [31]. Each parallel path consists of a TGP2100 5-b phase shifter and TGA2595 GaN PA. The output of each parallel path PA is connected to antenna subarray (unit cell) of four elements in 2×2 configuration [32]. The unit cell spacing is λ. The isolation between the individual antenna ports is below -30 dB. This means that the impact of active load modulation on the PA nonlinear behavior due to mutual coupling is small. Therefore, mutual coupling impacts are not considered in our analysis. So, in our platform, the dominant sources of PA nonlinear characteristic variation are the phase shifters' amplitude errors and the PAs themselves. The DPD object is created by measuring the nonlinear response of the DUT. In this case, the DUT consists of multiple parallel nonlinear PA branches. For SDPD training, a common feedback line is used to collect individual PA branch responses similarly as in [17] and [18]. The feedback line is a microstrip line to which the output of each PA is coupled. The individual branches are enabled one at a time through their time division duplex (TDD) switches. The coupled branch responses in the feedback path have a different delay and gain due to different lengths from PA output to the feedback path output. Therefore, the feedback signals are normalized against the common input

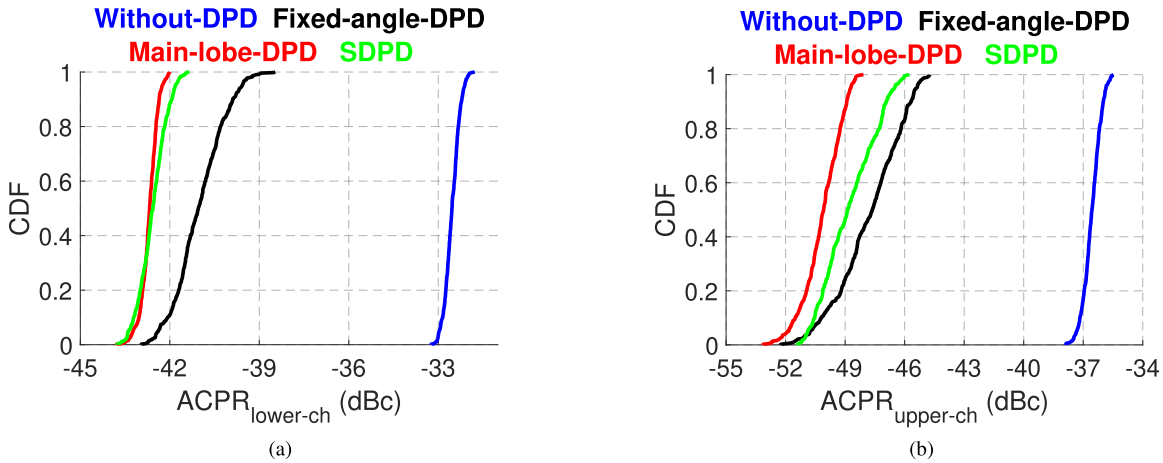

(a) (b)

Fig. 9. Simulated DPD performance in terms of ACPR over 1000 MC trials in the presence of amplitude variations due to phase shifters. (a) CDF of $\text{ACPR}_{\text{Lower-ch}}$. (b) CDF of $\text{ACPR}_{\text{Upper-ch}}$.

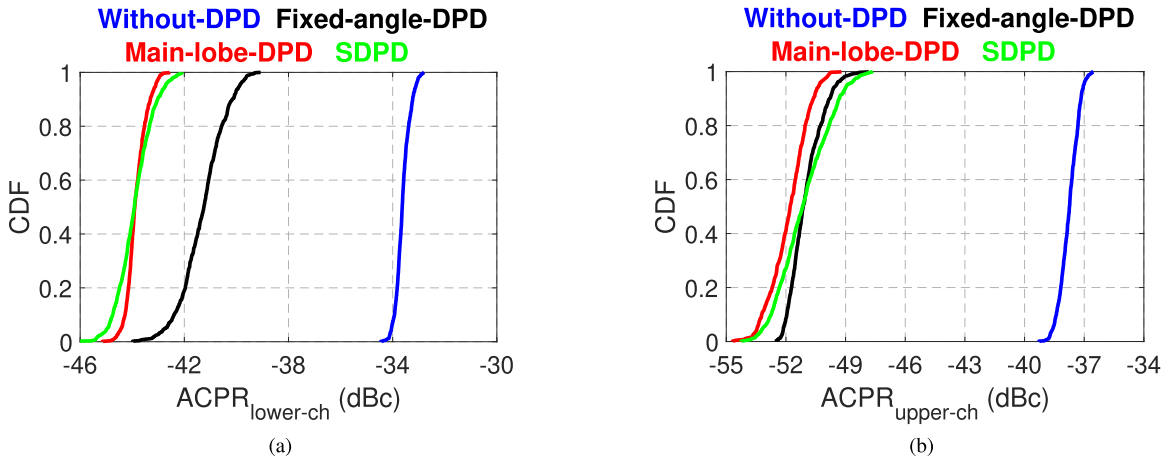

(a) (b)

Fig. 10. Simulated DPD performance in terms of ACPR over 1000 MC trials in the presence of amplitude variations due to ZF beamforming. (a) CDF of $\text{ACPR}_{\text{Lower-ch}}$. (b) CDF of $\text{ACPR}_{\text{Upper-ch}}$.

signal, for phase-coherent combining of the coefficients in (15) in the virtual array block.

B. OTA Measurement Setup

A photograph of the OTA measurement setup in an anechoic chamber is shown in Fig. 11. A 100-MHz wide, 64 QAM CP OFDM signal is generated in MATLAB and fed to the Keysight M8190A arbitrary waveform generator (ARB). The used waveform has a peak-to-average power ratio of 10.9 dB. The Keysight E8257B programmable signal generator (PSG) upconverts the baseband signal to the intermediate frequency (IF) that is fed to the DUT. The DUT has its own microcontroller unit for regulating the LO, phase shifters, attenuators, and PA biasing. The DUT is placed on a rotary table for azimuth domain beam measurements with a 1° angular resolution.

For the RX, we use the A-info LB-28-15 standard gain horn antenna placed at a distance of 2 m from the DUT. A preamplifier CA2630-141 is used to amplify the signal before the Keysight N9040B signal analyzer (UXA). Vector signal analyzer (VSA) software is used to collect the waveform

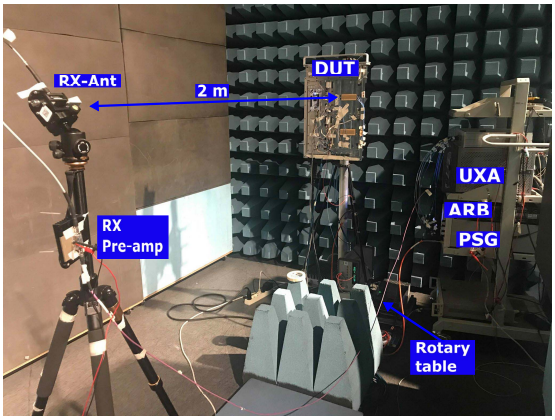

Fig. 11. OTA measurement setup placed in an anechoic chamber.

from the UXA. All the measurement equipment and DUT are controlled from MATLAB. In the analysis of the results, the free space path loss, cable losses, gain of the RX antenna, and preamplifier gain are removed.

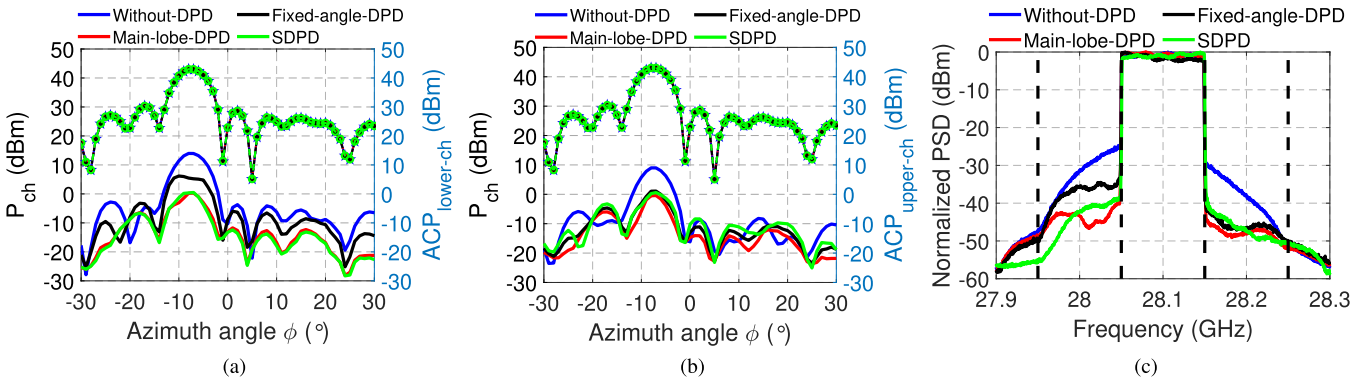

Fig. 12. Measured beams and spectrum at $\phi_s = -10°$. (a) Channel power and $\text{ACPR}_{\text{Lower-ch}}$. (b) Channel power and $\text{ACPR}_{\text{Upper-ch}}$. (c) Spectrum.

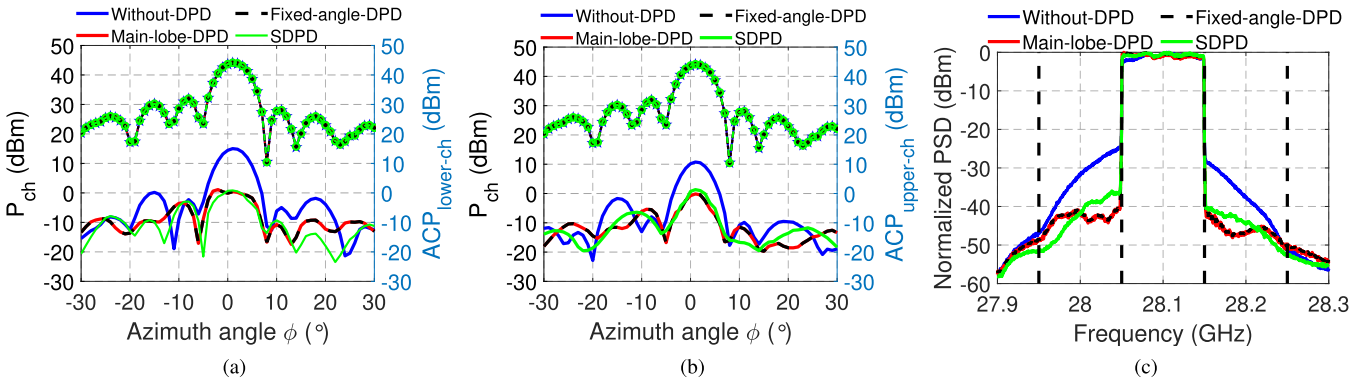

Fig. 13. Measured beams and spectrum at $\phi_s = 0°$. (a) Channel power and $\text{ACPR}_{\text{Lower-ch}}$. (b) Channel power and $\text{ACPR}_{\text{Upper-ch}}$. (c) Spectrum.

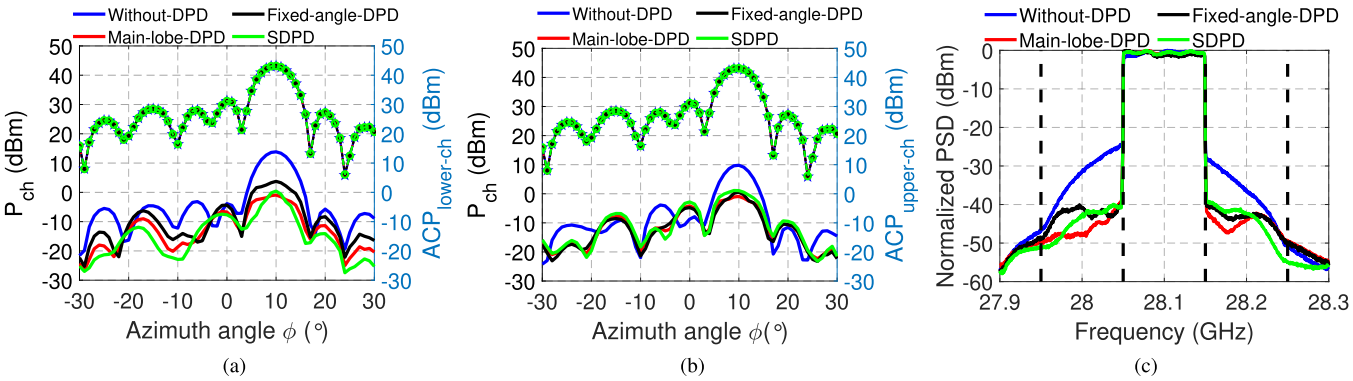

Fig. 14. Measured beams and spectrum at $\phi_s = 10°$. (a) Channel power and $\text{ACPR}_{\text{Lower-ch}}$. (b) Channel power and $\text{ACPR}_{\text{Upper-ch}}$. (c) Spectrum.

C. Measurement Results

The performance of the proposed SDPD is evaluated in different steering angles. The SDPD relies on the one-time training of the DPD coefficients and it uses the statistical information of the power variations in the DUT resulting from beamforming variations. For comparison, we use two other DPD techniques that rely on the OTA RX antenna for the training of the DPD coefficients, similar to the ones used in the simulation example of Section IV. These techniques are denoted as: 1) fixed-angle DPD and 2) main-lobe DPD. In 1), the OTA RX antenna is placed at a fixed location, and the DPD is trained from a fixed steering angle (in our measurements to $\phi_s = 0°$). The same coefficients are used for all the steering angles. In 2), the main-lobe DPD coefficients are trained for each steering angle by measuring the OTA array response in the main lobe. The main-lobe DPD is the optimal case in terms of DPD performance, but it is not a practical approach because the OTA RX must be placed in the main beam of the array. With beamsteering, this is a practical limitation of the main-lobe DPD implementation. The performance evaluation metrics used are the ACPR, error vector magnitude (EVM), and total radiated adjacent channel power ratio (TRACPR). The TRACPR is calculated as the ratio of total radiated adjacent channel power (TRACP) and total radiated main channel power (TRCP) [18].

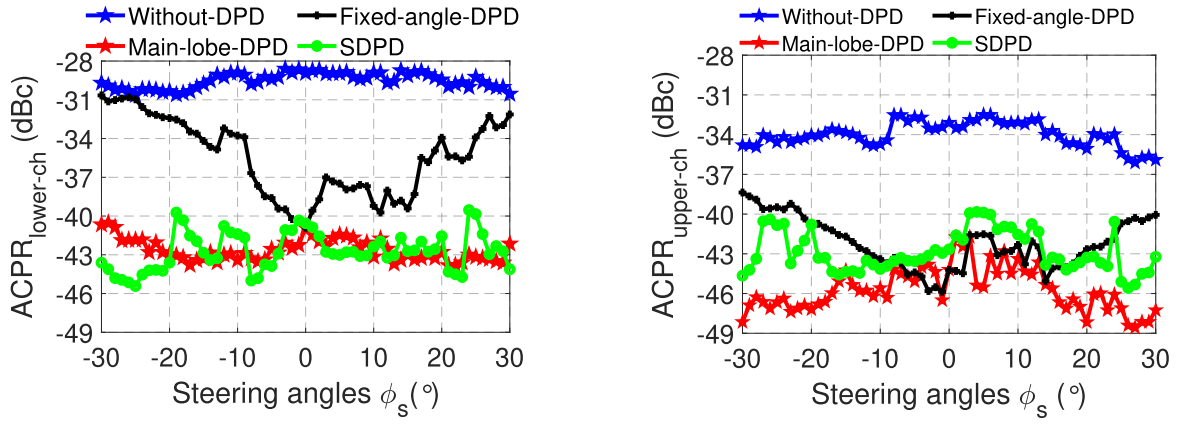

Fig. 15. Measured ACPR versus steering angle with different DPD methods. (a) $\text{ACPR}_{\text{Lower-ch}}$. (b) $\text{ACPR}_{\text{Upper-ch}}$.

1) DPD Performance at the Steering Angle: The radiated power in the main channel, adjacent channels (upper and lower), and their corresponding spectrum at steering angles $-10°$, $0°$, and $10°$ are plotted in Figs. 12–14, respectively. The beam of the main channel indicates that all the three DPD methods do not have a significant impact on the main beam. The maximum achieved EIRP at steering angle $\phi_s = 0°$ is around 44 dBm. From the figures, the main-lobe DPD gives the best performance because its coefficients are updated for each steering angle. Due to the continuous update of the DPD coefficients, the nonlinear distortion is minimized in all the beamsteering directions. On the other hand, the fixed-angle DPD is trained toward $\phi_s = 0°$ and the same DPD coefficients are used for other steering angles without retraining. The performance of the fixed-angle DPD is optimized only for the steering angle for which it is trained. The fixed-angle DPD performance deteriorates toward other steering angles because, with beamsteering, the control word-dependent gain of the phase shifters changes the PA nonlinear characteristics, and thus the array nonlinear behavior changes. To cope with the varying array nonlinear response, the DPD needs retraining. The SDPD uses the statistical information of power variations at the parallel PA inputs in the virtual array as shown in Fig. 7, to estimate the average array response. As shown in Fig. 2, the power variation due to phase shifters follows a normal distribution. Thus, for a small array size, the array response is more random due to less averaging effects. However, when the number of PA branches increases, the array behavior tends to be more predictable. This is because a large number of branches average the model toward the expected one, due to the law of large numbers. Thus, the SDPD performs well for large number of antenna elements (number of antenna elements ≥ 16) [27]. Similarly, the array beam in the adjacent channels is almost similar for the main-lobe DPD and SDPD cases. On the contrary, the power in the lower adjacent channel for fixed-angle DPD is relatively high. It can be clearly depicted in the spectrum figures.

Furthermore, the linearization performance of the three DPD methods in terms of ACPRs (lower and upper channels) is shown in Fig. 15. The performance is evaluated over steering angles $\phi_s \in \bigcup(-30°,\ 30°)$, in the azimuth domain, where $\bigcup$ denotes uniform distribution. Moreover, the performance of the tested DPD methods is also evaluated in terms of EVM and is shown in Fig. 16. The figure shows that all the three DPD methods improve the EVM in the main lobe in different steering directions. It is worth noting that the EVM values of the fixed-angle DPD method follow the same trend as that of the ACPR values of Fig. 15.

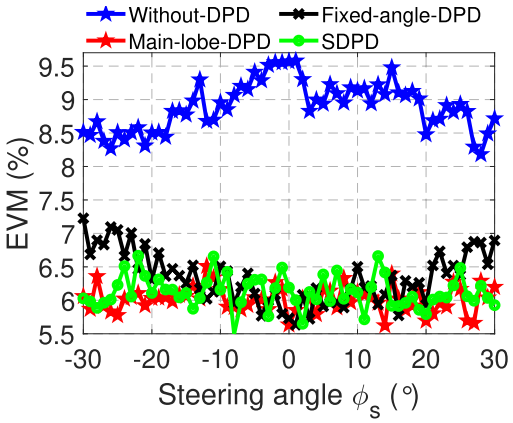

Fig. 16. Measured EVM versus steering angle with different DPD methods.

These measurement results indicate that the SDPD method outperforms the fixed-angle DPD method and provides comparable performance to the main-lobe DPD method using one-time trained DPD coefficients. Contrary to the SDPD, the main-lobe DPD relies on the continuous update of the DPD coefficients in all beamforming directions. The ACPR, TRACPR, and EVM results for the three DPD methods at the steering angles $-10°$, $0°$, and $10°$ are summarized in Table I.

2) Statistical Performance With Random Steering Angle: To further validate the performance of the proposed SDPD method over a longer measurement period, we conducted DPD performance measurements over 700 random steering angles selected from the range $\phi_s \in \bigcup(-30°,\ 30°)$ in the azimuth domain. In each of the 700 rounds, the main-lobe DPD coefficients are updated based on the measured array

TABLE I

MAIN LOBE ACPRS, TRACPRS, AND EVM WITH THREE DIFFERENT STEERING ANGLES. SUBINDICES L AND U STAND FOR LOWER AND UPPER ADJACENT CHANNELS, RESPECTIVELY

DPD	FoM	$\phi_s = -10°$	$\phi_s = 0°$	$\phi_s = 10°$
Without-DPD	$ACPR_L$	−28.9 dB	−28.9 dB	−28.9 dB
	$ACPR_U$	−34.7 dB	−33.1 dB	−33.0 dB
	$TRACPR_{max}$	−29.3 dB	−29.3 dB	−29.7 dB
	EVM	8.9 %	9.5 %	9.1 %
Main-lobe-DPD	$ACPR_L$	−43.4 dB	−40.9 dB	−43.1 dB
	$ACPR_U$	−45.5 dB	−44.2 dB	−43.3 dB
	$TRACPR_{max}$	−42.3 dB	−40.3 dB	−41.7 dB
	EVM	6.1 %	5.6 %	6.1 %
Fixed-angle-DPD	$ACPR_L$	−33.7 dB	−40.9 dB	−39.2 dB
	$ACPR_U$	−43.4 dB	−44.2 dB	−42.3 dB
	$TRACPR_{max}$	−35.7 dB	−40.3 dB	−38.3 dB
	EVM	6.5 %	5.7 %	6.5 %
SDPD	$ACPR_L$	−41.4 dB	−40.5 dB	−42.3 dB
	$ACPR_U$	−44.1 dB	−42.6 dB	−41.5 dB
	$TRACPR_{max}$	−41.1 dB	−41.4 dB	−40.3 dB
	EVM	6.1 %	6.1 %	6.1 %

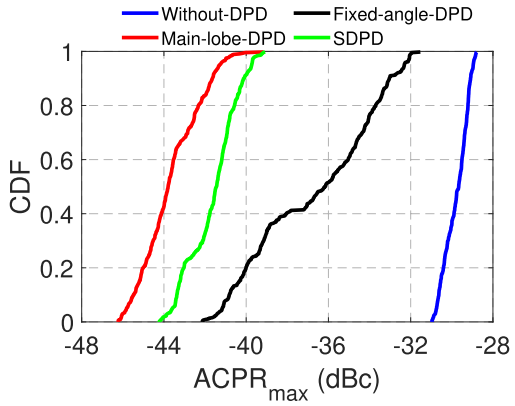

Fig. 17. Empirical CDFs of $ACPR_{max}$ measured over 700 random steering angles.

response in the far-field in the beamsteering direction. The SDPD and fixed-angle DPD methods use the one-time calculated DPD coefficients. The obtained cdf of the $ACPR_{max} = \max(ACPR_{lower\text{-}ch}, ACPR_{upper\text{-}ch})$ for the DPD methods is shown in Fig. 17. From the figure, it can be seen that the fixed-angle DPD performance worsens with the changes in the beamsteering directions. This is because the fixed-angle DPD is trained for one realization of beamforming coefficients and does not take into account the impact of the variations in the radiated array nonlinear behavior with beamforming. Contrary to this, the SDPD method can guarantee better performance with high reliability and with one-time trained DPD coefficients. This means that the DPD can be made less susceptible to beamforming in large arrays, provided that the statistical information of the beamforming variations are used in extracting the DPD object. Furthermore, the obtained cdf of EVM values over the 700 measurement rounds is shown in Fig. 18. According to the 5G NR FR2 specifications, the TX EVM requirement for the successful transmission of 64 QAM is 8% or better. The three tested DPD methods provide better performance than the acceptable threshold, with the main-lobe DPD providing the best performance among the tested DPD methods. The SDPD method provides comparable performance to that of the main-lobe DPD. It is worth noting that the presented measurement results indicate that

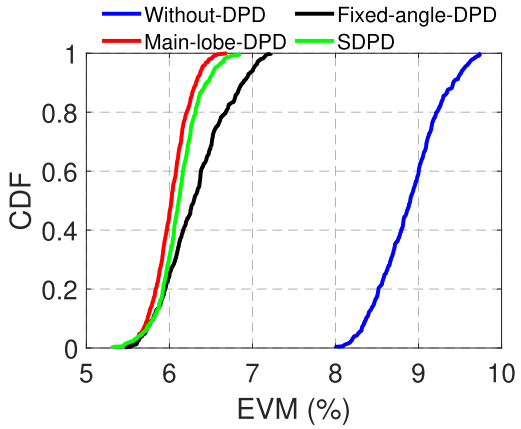

Fig. 18. Empirical cdf of EVM measured over 700 random steering angles.

the performance of the SDPD slightly deteriorates to some steering angles compared with that of the main-lobe DPD. This means that with the proposed method, the linearization performance cannot be optimized to every steering direction individually as only one set of DPD coefficients are used. On the other hand, the SDPD provides decent linearization performance across a wide range of steering angles without the necessity of readapting the DPD coefficients to all steering angles. Moreover, the slight variation in the performance of SDPD can be afforded, given that the performance adheres to the specification requirements, which are relaxed for 3GPP 5GNR.

VI. CONCLUSION

Linearization of mmWave RF beamforming TX is performed through SISO DPD models due to the shared digital input. The SISO-based DPD models require a continuous update of the DPD coefficients with the changes in the beamforming directions, due to the radiated array nonlinear behavior dependency on beamforming coefficients. Especially if the beamforming angle changes randomly for every slot, very fast DPD adaptation is required to enable good linearity. To address the DPD coefficients' retraining problem, we proposed the SDPD method. It is based on individual PA branch measurements through shared feedback. Along with the shared feedback path, the proposed DPD method uses the statistical information of the beamforming variations in the array to measure the power adaptive model per branch and ultimately estimate the average array response. The estimated response is used for DPD object extraction. The proposed DPD method takes advantage of the averaging effect in the beamforming array, i.e., when the number of varying parallel nonlinear branches is large, the array behavior tends to be more predictable. Therefore, the SDPD coefficients are one-time trained using the estimated average array response instead of the conventional training mechanisms that rely on direction-dependent array response. Thus, the SDPD alleviates the retraining problem of the DPD coefficients and is less susceptible to beamforming variations. The performance of the proposed SDPD method is evaluated in the presence of beamforming variations. The performance evaluation is carried out in both simulations and measurements of 28-GHz phased

array transceiver over different steering angles. The presented measurement result indicates that the proposed SDPD method can provide decent linearization performance even when the instantaneous beamforming-dependent array response is not known. This means that the array linearization process can be simplified further toward an offline trained or factory measurement-based power adaptive model and take the statistical information of the beamforming variations into account when extracting the DPD object. The presented approach can be an attractive solution for the practical implementation of DPD especially for large arrays and can fulfill the 3GPP NR ACPR, EVM, and TRACPR requirements.

ACKNOWLEDGMENT

The authors would like to thank Keysight Technologies for laboratory equipment.

REFERENCES

[1] T. S. Rappaport *et al.*, "Millimeter wave mobile communications for 5G cellular: It will work!" *IEEE Access*, vol. 1, pp. 335–349, 2013.
[2] M. Latva-Aho and K. Leppänen, *Key Drivers and Research Challenges for 6G Ubiquitous Wireless Intelligence*. Oulu, Finland: Univ. Oulu, 2019.
[3] I. F. Akyildiz, C. Han, and S. Nie, "Combating the distance problem in the millimeter wave and terahertz frequency bands," *IEEE Commun. Mag.*, vol. 56, no. 6, pp. 102–108, Jun. 2018.
[4] L. Guan and A. Zhu, "Green communications: Digital predistortion for wideband RF power amplifiers," *IEEE Microw. Mag.*, vol. 15, no. 7, pp. 84–99, Nov./Dec. 2014.
[5] B. Fehri and S. Boumaiza, "Baseband equivalent Volterra series for behavioral modeling and digital predistortion of wideband transmitters," U.S. Patent 9 727 677 B2, Jul. 8, 2017.
[6] J. Xiong, X. Wang, T. Duan, and J. Wang, "Digital predistortion parameter obtaining method and pre-distortion system," U.S. Patent 9 647 717 B2, May 9, 2017.
[7] F. M. Ghannouchi and O. Hammi, "Behavioral modeling and predistortion," *IEEE Microw. Mag.*, vol. 10, no. 7, pp. 52–64, Dec. 2009.
[8] N. Kelly, W. Cao, and A. Zhu, "Preparing linearity and efficiency for 5G: Digital predistortion for dual-band Doherty power amplifiers with mixed-mode carrier aggregation," *IEEE Micro. Mag.*, vol. 18, no. 1, pp. 76–84, Feb. 2017.
[9] C. Fager, K. Hausmair, K. Buisman, K. Andersson, E. Sienkiewicz, and D. Gustafsson, "Analysis of nonlinear distortion in phased array transmitters," in *Proc. Integr. Nonlinear Microw. Millimetre-Wave Circuits Workshop (INMMiC)*, Apr. 2017, pp. 1–4.
[10] F. M. Barradas, T. R. Cunha, P. M. Cabral, and J. C. Pedro, "Modeling PA linearity and efficiency in MIMO transmitters," in *IEEE MTT-S Int. Microw. Symp. Dig.*, Jun. 2017, pp. 1999–2002.
[11] E. Ng, Y. Beltagy, G. Scarlato, A. Ben Ayed, P. Mitran, and S. Boumaiza, "Digital predistortion of millimeter-wave RF beamforming arrays using low number of steering angle-dependent coefficient sets," *IEEE Trans. Microw. Theory Techn.*, vol. 67, no. 11, pp. 4479–4492, Nov. 2019.
[12] N. Tervo *et al.*, "Digital predistortion concepts for linearization of mmW phased array transmitters," in *Proc. 16th Int. Symp. Wireless Commun. Syst. (ISWCS)*, Aug. 2019, pp. 325–329.
[13] C. Fager, T. Eriksson, F. Barradas, K. Hausmair, T. Cunha, and J. C. Pedro, "Linearity and efficiency in 5G transmitters: New techniques for analyzing efficiency, linearity, and linearization in a 5G active antenna transmitter context," *IEEE Microw. Mag.*, vol. 20, no. 5, pp. 35–49, May 2019.
[14] F. Jalili, F. F. Tafuri, O. K. Jensen, Y. Li, M. Shen, and G. F. Pedersen, "Linearization trade-offs in a 5G mmWave active phased array OTA setup," *IEEE Access*, vol. 8, pp. 110669–110677, 2020.
[15] S. Lee *et al.*, "Digital predistortion for power amplifiers in hybrid MIMO systems with antenna subarrays," in *Proc. IEEE 81st Veh. Technol. Conf. (VTC Spring)*, May 2015, pp. 1–5.
[16] N. Tervo, J. Aikio, T. Tuovinen, T. Rahkonen, and A. Parssinen, "Digital predistortion of amplitude varying phased array utilising over-the-air combining," in *IEEE MTT-S Int. Microw. Symp. Dig.*, Jun. 2017, pp. 1165–1168.
[17] N. Tervo *et al.*, "Digital predistortion of millimeter-wave phased array transmitter with over-the-air calibrated simplified conductive feedback architecture," in *IEEE MTT-S Int. Microw. Symp. Dig.*, Aug. 2020, pp. 543–546.
[18] N. Tervo *et al.*, "Digital predistortion of phased-array transmitter with shared feedback and far-field calibration," *IEEE Trans. Microw. Theory Techn.*, vol. 69, no. 1, pp. 1000–1015, Jan. 2021.
[19] N. Tervo, M. E. Leinonen, J. Aikio, T. Rahkonen, and A. Pärssinen, "Analyzing the effects of PA variations on the performance of phased array digital predistortion," in *Proc. IEEE 29th Annu. Int. Symp. Pers., Indoor Mobile Radio Commun. (PIMRC)*, Sep. 2018, pp. 215–219.
[20] M. Abdelaziz, L. Antilla, A. Brihuega, F. Tufvesson, and M. Valkama, "Digital predistortion for hybrid MIMO transmitters," *IEEE J. Sel. Topics Signal Process.*, vol. 12, no. 3, pp. 445–454, Jun. 2018.
[21] K. Hausmair, P. N. Landin, U. Gustavsson, C. Fager, and T. Eriksson, "Digital predistortion for multi-antenna transmitters affected by antenna crosstalk," *IEEE Trans. Microw. Theory Techn.*, vol. 66, no. 3, pp. 1524–1535, Mar. 2018.
[22] X. Wang, C. Yu, Y. Li, W. Hong, and A. Zhu, "Real-time single channel over-the-air data acquisition for digital predistortion of 5G massive MIMO wireless transmitters," in *IEEE MTT-S Int. Microw. Symp. Dig.*, May 2019, pp. 1–3.
[23] X. Liu *et al.*, "Beam-oriented digital predistortion for 5G massive MIMO hybrid beamforming transmitters," *IEEE Trans. Microw. Theory Techn.*, vol. 66, no. 7, pp. 3419–3432, Jul. 2018.
[24] X. Liu, W. Chen, L. Chen, F. M. Ghannouchi, and Z. Feng, "Linearization for hybrid beamforming array utilizing embedded over-the-air diversity feedbacks," *IEEE Trans. Microw. Theory Techn.*, vol. 67, no. 12, pp. 5235–5248, Dec. 2019.
[25] X. Wang, Y. Li, C. Yu, W. Hong, and A. Zhu, "Digital predistortion of 5G massive MIMO wireless transmitters based on indirect identification of power amplifier behavior with OTA tests," *IEEE Trans. Microw. Theory Techn.*, vol. 68, no. 1, pp. 316–328, Jan. 2020.
[26] B. Khan, N. Tervo, A. Parssinen, and M. Juntti, "Average linearization of phased array transmitters under random amplitude and phase variations," in *Proc. 16th Int. Symp. Wireless Commun. Syst. (ISWCS)*, Aug. 2019, pp. 553–557.
[27] B. Khan, N. Tervo, A. Parssinen, and M. Juntti, "Statistical linearization of phased arrays using power adaptive power amplifier model," in *Proc. IEEE 30th Annu. Int. Symp. Pers., Indoor Mobile Radio Commun. (PIMRC)*, Sep. 2019, pp. 1–5.
[28] O. Kursu *et al.*, "Design and measurement of a 5G mmW mobile backhaul transceiver at 28 GHz," *EURASIP J. Wireless Commun. Netw.*, vol. 2018, no. 1, pp. 1–11, Aug. 2018.
[29] M. Majidzadeh, A. Moilanen, N. Tervo, H. Pennanen, A. Tolli, and M. Latva-aho, "Partially connected hybrid beamforming for large antenna arrays in multi-user MISO systems," in *Proc. IEEE 28th Annu. Int. Symp. Pers., Indoor, Mobile Radio Commun. (PIMRC)*, Oct. 2017, pp. 1–6.
[30] Y. Guo, C. Yu, and A. Zhu, "Power adaptive digital predistortion for wideband RF power amplifiers with dynamic power transmission," *IEEE Trans. Microw. Theory Techn.*, vol. 63, no. 11, pp. 3595–3607, Nov. 2015.
[31] M. E. Leinonen, G. Destino, O. Kursu, M. Sonkki, and A. Pärssinen, "28 GHz wireless backhaul transceiver characterization and radio link budget," *ETRI J.*, vol. 40, no. 1, pp. 89–100, Feb. 2018.
[32] M. Sonkki *et al.*, "Linearly polarized 64-element antenna array for mm-wave mobile backhaul application," in *Proc. 12th Eur. Conf. Antennas Propag. (EuCAP)*, 2018, pp. 1–5.

Bilal Khan (Graduate Student Member, IEEE) received the B.Sc. degree in electrical engineering (communication) from the University of Engineering and Technology Peshawar, Peshawar, Pakistan, in 2013, and the M.Sc. degree in wireless communication engineering from the University of Oulu, Oulu, Finland, in 2016, where he is currently pursuing the Ph.D. degree.

His research interests include digital predistortion for radio frequency (RF) power amplifiers with an emphasis on robust and simplified linearization solutions for multiantenna transmitters in millimeter-wave systems.

Nuutti Tervo (Member, IEEE) received the B.Sc. (Tech.), M.Sc. (Tech.), and D.Sc. (Tech.) degrees (Hons.) from the University of Oulu, Oulu, Finland, in 2014 and 2022, respectively. His Ph.D. dissertation research focused on nonlinearity and linearization of millimeter-wave beamforming transceivers.

Since 2022, he has been working as a Post-Doctoral Researcher with the Centre for Wireless Communications—Radio Technologies (CWC-RT) Research Unit, University of Oulu. He has a strong background in different fields of wireless communications, including radio frequency (RF), radio channel modeling, signal processing, and system-level analysis. Around those topics, he has already authored or coauthored more than 55 international journal articles and conference papers and he holds patents.

Dr. Tervo was a recipient of the Young Scientist Award of the URSI XXXV Finnish Convention on Radio Science, Tampere, Finland, in 2019. In 2020, he has coauthored the paper that won the 50th EuMC Microwave Prize 2020, Utrecht, The Netherlands.

Markku Jokinen received the M.Sc. degree in electronics from the University of Oulu, Oulu, Finland, in 2010, where he is currently pursuing the Ph.D. degree with a focus on measurement techniques.

He is currently working as the Research Scientist of the Centre for Wireless Communications, University of Oulu. He has gained experience in the design and implementation of wireless system algorithms and protocols with software-defined radio platforms.

Aarno Pärssinen (Senior Member, IEEE) received the M.Sc. degree, the Licentiate degree in technology, and the D.Sc. degree in electrical engineering from the Helsinki University of Technology, Espoo, Finland, in 1995, 1997, and 2000, respectively.

From 1994 to 2000, he was with the Electronic Circuit Design Laboratory, Helsinki University of Technology, working on direct conversion receivers and subsampling mixers for wireless communications. In 1996, he was a Research Visitor at the University of California at Santa Barbara, Santa Barbara, CA, USA. From 2000 to 2011, he was with Nokia Research Center, Helsinki, Finland. From 2009 to 2011, he has served as a member of Nokia CEO Technology Council. From 2011 to 2013, he has worked as a Distinguished Researcher and the Radio Frequency (RF) Research Manager of Renesas Mobile Corporation, Helsinki. From October 2013 to September 2014, he was the Associate Technical Director of Broadcom, Helsinki. Since September 2014, he has been with the Centre for Wireless Communications, University of Oulu, Oulu, Finland, where he is currently a Professor. He leads devices and circuits research area in 6G flagship program financed by the Academy of Finland. He has authored or coauthored one book, two book chapters, more than 180 international journal articles and conference papers, and holds several patents. His research interests include wireless systems and transceiver architectures for wireless communications with a special emphasis on RF and analog integrated circuit and system design.

Dr. Pärssinen was a recipient of the European Microwave Price on the Best Paper of the European Microwave Conference 2020. He is also one of the original contributors to Bluetooth low-energy extension, now called as BT LE. He has served as a member for the Technical Program Committee of International Solid-State Circuits Conference from 2007 to 2017, where he was the Chair of the European Regional Committee from 2012 to 2013 and the Chair of the Wireless Sub-Committee from 2014 to 2017. He has been serving as the Solid-State Circuits Society Representative for IEEE 5G Initiative from 2015 to 2019.

Markku Juntti (Fellow, IEEE) received the M.Sc. and Dr.Sc. degrees in electrical engineering (EE) from the University of Oulu, Oulu, Finland, in 1993 and 1997, respectively.

He was with the University of Oulu from 1992 to 1998. In academic year 1994–1995, he was a Visiting Scholar with Rice University, Houston, TX, USA. From 1999 to 2000, he was the Senior Specialist of Nokia Networks, Oulu. Since 2000, he has been a Professor of communications engineering with the Centre for Wireless Communications (CWC), University of Oulu, where he leads the Communications Signal Processing (CSP) Research Group. He also serves as Head of the CWC—Radio Technologies (RT) Research Unit. He is also an Adjunct Professor with the Department of Electrical and Computer Engineering, Rice University. He is the author or a coauthor in almost 500 papers published in international journals and conference records as well as in books *Wideband CDMA for UMTS* from 2000 to 2010, *Handbook of Signal Processing Systems* in 2013 and 2018, and *5G Wireless Technologies* in 2017. His research interests include signal processing for wireless networks as well as communication and information theory.

Dr. Juntti was the Secretary of IEEE Communication Society Finland Chapter from 1996 to 1997 and the Chairman from 2000 to 2001. He has been the Secretary of the Technical Program Committee (TPC) of the 2001 IEEE International Conference on Communications (ICC), and the Chair or the Co-Chair of the Technical Program Committee of several conferences, including 2006 and 2021 IEEE International Symposium on Personal, Indoor and Mobile Radio Communications (PIMRC), the Signal Processing for Communications Symposium of IEEE Globecom 2014, Symposium on Transceivers and Signal Processing for 5G Wireless and mm-Wave Systems of IEEE GlobalSIP 2016, ACM NanoCom 2018, and 2019 International Symposium on Wireless Communication Systems (ISWCS). He has also served as the General Chair for 2011 IEEE Communication Theory Workshop (CTW 2011) and 2022 IEEE Workshop on Signal Processing Advances in Wireless Communications (SPAWC). He is an Editor of IEEE TRANSACTIONS ON WIRELESS COMMUNICATIONS, and served previously in similar role in IEEE TRANSACTIONS ON COMMUNICATIONS and IEEE TRANSACTIONS ON VEHICULAR TECHNOLOGY.